Observations of Cygnus X#1 with the EXITE2 Hard X#Ray Balloon Payload

The Astrophysical Journal, 618:856–865, 2005 January 10

OBSERVATIONS OF CYGNUS X-1 WITH THE EXITE2 HARD X-RAY BALLOON PAYLOAD

Y. Chou,[1] P. F. Bloser,[2] J. E. Grindlay,[3] and T. Narita[4]

Received 2001 August 28; accepted 2004 February 6

ABSTRACT

We present results from the second-generation Energetic X-ray Imaging Telescope (EXITE2) observations of the black hole X-ray binary Cyg X-1 during the experiment's 1997 and 2001 flights. The EXITE2 phoswich [NaI(Tl)/CsI(Na)] detector is designed to image cosmic X-ray sources in the hard X-ray band by using the coded-aperture imaging technique from a high-altitude scientific balloon. The sky image reconstruction methodology used for EXITE2 is also discussed in detail. Background reduction (PSD rejection), subtractive flat-fielding, pixel shuffling, and image functions are introduced. During the observations from the EXITE2 1997 and 2001 flights, Cyg X-1 is easily detected in the 37–237 keV energy range. During the 1997 observations, the spectrum is well fitted by a Comptonization model. The spectral signatures and the observed 100 keV flux, together with the *RXTE* ASM light curve, indicate that the source was in the typical low state during this observation. Evidence is seen for hard X-ray variability on timescales on the order of 10 minutes. During the 2001 flight the spectrum is best fit by an extended power law with no observable cutoff. This is possible evidence of a transition to the high state, which is indeed seen in the *RXTE* ASM light curve shortly after our observation.

Subject headings: stars: individual (Cygnus X-1) — X-rays: binaries — X-rays: individual (Cygnus X-1)

1. INTRODUCTION

The hard X-ray band (20–600 keV) provides a window into $\sim 10^9$ K thermal and nonthermal phenomena, such as high-energy synchrotron radiation, magnetic cyclotron absorption and emission, and inverse Compton scattering of cosmic X-ray sources. Hard X-ray imaging telescopes provide a significant improvement in sensitivity and angular resolution over non-imaging telescopes. Grazing-incidence mirror–focusing telescopes commonly employed for the soft X-ray band are being developed for hard X-ray telescope use up to ~100 keV. The coded aperture imaging telescope technique (Caroli et al. 1987, and references therein) has been widely applied to hard X-ray and soft gamma-ray imaging telescopes (e.g., the French SIGMA telescope, 30 keV–1.3 MeV; see Paul et al. 1991). This technique requires large area detectors with good spatial and spectral resolution.

In recent years, we have designed and developed a hard X-ray imaging coded aperture telescope with the second-generation Energetic X-ray Imaging Telescope Experiment (EXITE2, Lum et al. 1994; Manandhar 1995; Chou et al. 1998; Bloser et al. 2002; Chou 2001). The telescope detects and images cosmic X-ray sources in the hard X-ray band from a high-altitude balloon. At its core is a phoswich detector composed of a NaI(Tl) crystal surrounded by CsI(Na) crystals on five sides. A photomultiplier tube (PMT; a list of abbreviations is given in Table 1) array and processing electronics are applied to process the signals from the combined NaI/CsI crystal assembly. The electronic signals are first digitized, then transformed and stored in the on-board computer system (a 486 single-board computer [SBC]) and ground support equipment (GSE) for further analysis. The payload is carried by the scientific balloon, and the observations are made at ~125,000 feet (~38,000 m) float altitude from a gondola with an inertial pointing and aspect recording system.

The black hole X-ray binary Cygnus X-1 was observed during the EXITE2 1997 and 2001 flights. Cyg X-1 is one of the best-studied X-ray and gamma-ray sources in the sky, consisting of a black hole with mass >6 $M_\odot$ and an O-type blue supergiant companion. The source has long been known to spend ~90% of its time in the so-called "low" state, as defined by its 1–10 keV flux, with occasional forays into the "high" state (e.g., Priedhorsky et al. 1983). The low-state spectrum at hard X-ray energies (>30 keV) has been well described by many authors using a thermal Comptonization model (Sunyaev & Titarchuk 1980) with electron temperature $kT_e \sim 30$–80 keV and optical depth $\tau \sim 2$–5. Using *HEAO-3* data, Ling et al. (1987) further subdivided the low state into three levels based on the hard X-ray flux, denoted γ_1, γ_2, and γ_3 in order of increasing flux, and these remain useful points of comparison. The hard X-ray spectrum in the high state is characterized by a soft power law (photon spectral index 2.2–3) with no cutoff below several hundred keV and a lower overall hard X-ray flux, as is typical of black hole X-ray binaries (Grove et al. 1998; Esin et al. 1998). Physically, the high-energy spectrum of Cyg X-1, like that of most black hole X-ray binaries, is widely accepted to originate from the combination of a geometrically thin, optically thick accretion disk, radiating thermally in the soft X-ray band, and a geometrically thick, optically thin hot corona, which upscatters the soft photons from the disk into the observed Comptonized hard X-ray spectrum. The transitions between the low and high state are believed to be caused by a shift in the relative sizes of the disk and corona, brought on by a change in the accretion rate (see, for example, Esin et al. 1998). In this paper, we present the results for the EXITE2 hard X-ray observations of

[1] Graduate Institute of Astronomy, National Central University, No. 300, Jung-da Road, Jung-li City, Tuoyuan 320, Taiwan; yichou@astro.ncu.edu.tw.
[2] NASA Goddard Space Flight Center, Code 661, Greenbelt, MD 20771; bloser@milkyway.gsfc.nasa.gov.
[3] Harvard-Smithsonian Center for Astrophysics, 60 Garden Street, Cambridge, MA 02138; josh@head-cfa.harvard.edu.
[4] Department of Physics, College of the Holy Cross, 1 College Street, Worcester, MA 01610; tnarita@holycross.edu.

TABLE 1
List of Abbreviations

Abbreviation	Name
Amcal	^{241}Am Calibration Source
ARF	Ancillary Response File
CAL	Calibration Event
DAT	Digital Audio Tape
EXITE	Energetic X-ray Imaging Telescope Experiment
GSE	Ground Support Equipment
LED	Light-Emitting Diode
MLM	Maximum Likelihood Method
PHA	Pulse Height Analyzer
PMT	Photomultiplier Tube
PSD	Pulse-Shape Discrimination
PSF	Point Spread Function
RMF	Redistribution Matrix File
SBC	Single-Board Computer
URA	Uniformly Redundant Array

Cyg X-1. Results for the Crab Nebula and 3C 273/GRS 1227+025 are given by Bloser et al. (2002) and Grindlay et al. (2005), respectively.

2. EXPERIMENT SETUP: DETECTOR ARCHITECTURE AND PROCESSING METHODOLOGY

EXITE2 is an imaging phoswich detector designed to observe astrophysical X-ray sources in the hard X-ray band (20–600 keV) with high spatial and spectral resolution. A similar, although larger, imaging phoswich (GRIP-2, cf. Schindler et al. 1997) was developed for balloon-borne observations extending to somewhat higher energy but with lower spatial/spectral resolution. The EXITE2 detector consists of a 36 cm $\times$ 36 cm $\times$ 1 cm NaI(Tl) scintillator surrounded on four sides and the rear by 2 cm thick CsI(Na) crystals. Using the different scintillation-light decay time constants for NaI(Tl) and CsI(Na), 230 and 680 ns, respectively, we are able to filter most of the background with a pulse-shape discriminator (PSD). PSD acceptance and rejection efficiencies are typically >90% (cf. Chou 2001 for derivation) and are listed in Table 2. The NaI/CsI crystals absorb the X-ray and generate scintillation light in proportion to the X-ray photon energy collected by a 7 $\times$ 7 PMT array. The light signals are subsequently amplified and converted into electronic pulses, which are then further amplified by the following preamplifiers before digitization. The rise times of the pulses (i.e., the decay time of scintillation light, or the PSD values) are measured by the time difference between the detector trigger time and the zero-crossing time of the sum of all pulses from the 49 PMT channels.

The gains and offsets of the 49 PMTs are continuously monitored and calibrated by the onboard calibration system during the flight. The system consists of four ^{241}Am sources and 12 light-emitting diodes (LEDs). The four ^{241}Am weak sources [$\sim$30 nCi (nanoCuries), hereafter Amcal] are placed at the bottom of the collimator to calibrate the gains of the four corner PMTs. Each Amcal source is dissolved into a small (3 mm diameter $\times$ 3 mm high cylinder) plastic scintillator from which the 5.5 MeV α-particle accompanying each 60 keV photon is detected by its scintillation light and read out through an optical fiber to an external PMT (4 Amcal fibers coupled to a single PMT; cf. Bloser 2000 for a detailed description). The gains on the other 45 PMTs (noncorner PMTs) are calibrated with the 12 LEDs that are mounted in a square (shown as Fig. 1) on the back of the phoswich crystal and pulsed on/off by a 130 Hz (or 2 Hz) square wave so that each LED fires at a rate $\frac{1}{13}$ of the total. The offsets are obtained from the "CAL" events when the system is triggered artificially to digitize current amplitude in each of the 49 channels.

The collimator is used to limit the detector view field to $4\overset{\circ}{.}65 \times 4\overset{\circ}{.}65$ (FWHM). The phoswich crystal assembly and PMT array are surrounded on five sides by active and passive shields with the active shields on the outside. The active shields consist of plastic scintillator (1 cm thick NE-102) each read out (edge-coupled through a triangular light guide) by a single PMT to detect the scintillation light output. Each detector event has a 16-bit validity word composed of validity bits from the shields, Amcal, LED and CAL tags, and other discriminators. The final digitized EXITE2 data (49 word pulse height + 5 word event time, validity, and PSD) are

TABLE 2
EXITE2 PSD Rejection and Acceptance Efficiencies

Energy Band	Energy Range (keV)	CsI(Na) Rejection Efficiency (%)	NaI(Tl) Acceptance Efficiency (%)
1[a]	10–20	...	...
2[b]	20–27	...	...
3	27–37	65	90
4	37–50	77	93
5	50–70	87	95
6	70–93	93	99
7	93–127	96	$\sim$100
8	127–174	92	$\sim$100
9	174–237	70	94
10	237–323	48	91
11	323–440	27	85
12[b]	440–600	...	...

[a] Empty band.
[b] No software PSD cut in this band because the NaI(Tl) and CsI(Na) events almost merge together in PSD spectrum.

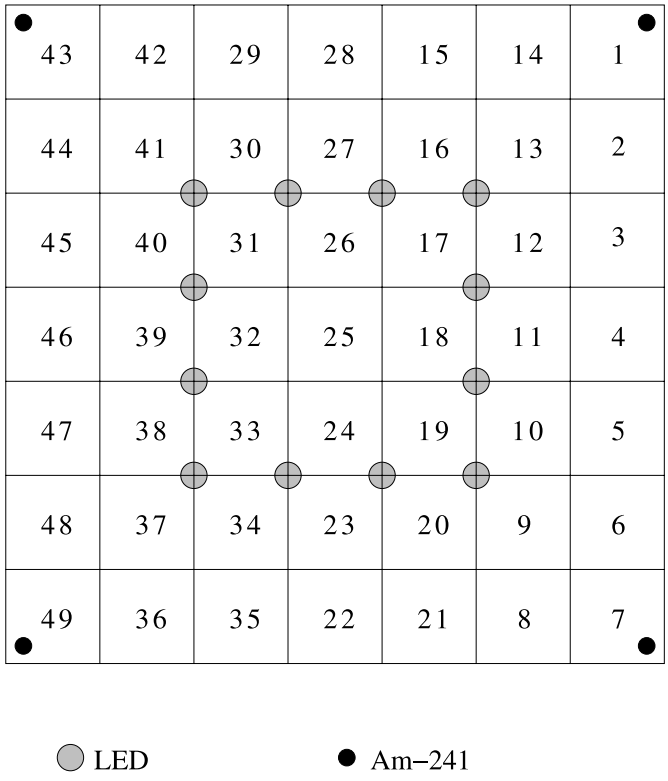

FIG. 1.—Relative positions of LEDs, Amcal sources, and PMTs (*squares*). The numbers inside the boxes are PMT indices.

recorded either on the onboard digital audio tape (DAT) recorder (1997 flight) or on the hard disk in the SBC (2001 flight) mounted on the gondola. A subset of the EXITE2 data (hereafter the telemetry data) is also transmitted to ground and recorded in the GSE along with the system housekeeping data. The data throughput and the effective live time is measured by the number of CAL events (2 or 130 Hz) recorded in the GSE data. Further details of EXITE2 detector performances (energy and spatial resolution, PSD calibration and efficiencies, detector imaging performances and calibration) are given by Chou et al. (1998) and Chou (2001).

3. OBSERVATIONS

The first EXITE2 science flight was launched from Fort Sumner, New Mexico on 1997 May 7 at UT 16:15. Overall, the flight was a success. With the exception of gain irregularities on PMTs 10 and 47, the detector worked as expected. The PMT gain decreases were first noted at UT 18:30. Because of the onboard calibration, the overall impact of the variations on the quality of the observation after calibration appeared to be small. The observations started at UT 19:15. The telescope was first oriented toward the Crab Nebula and subsequently toward the low-mass X-ray binary 4U 0614+09, QSO 3C 273, active galaxy NGC 4151 and Cyg X-1 during the ensuing ~15 hr flight.

The Cyg X-1 data were acquired between UT 07:50 and 09:58 on May 8. The pointing was stable with pointing offsets less than $30'$ during this period. However, there were two problems in this observation interval that affected data resolution. First, the SBC failed to record data on DAT (successful onboard DAT operation was achieved later in the flight). Second, the telemetry data were involuntarily switched to the data compression mode[5] at UT 08:38. The compression caused undesired image distortion near the low-gain PMT 47. To compensate for this distortion, the observation data are divided into two parts, according to the compression scheme, and are analyzed separately in this paper.

The 2001 EXITE2 flight was launched from Fort Sumner, New Mexico at UT16:23 on 2001 May 23. Just before the payload was launched, we found the SBC was not able to access the EXITE2 science data (because of a failed DSP interface board in the SBC pressure vessel—which could not be accessed just before launch). Therefore, only the real-time telemetry data could be obtained in this flight. In order to improve data throughput, we decided to record only the most sensitive energy bands (37–237 keV). The new discriminator settings increased the total throughput ratio from ~15% to ~40%. The telescope was pointing on Cyg X-1 from UT 08:20 to 09:54 (local time 02:20 to 03:54) on May 24. During the observation, the EXITE2 system worked as expected although the gain irregularities of PMTs 10 and 47, similar to the 1997 flight, were still seen during the flight. The data analysis methods are described in § 4 and results for Cyg X-1 from the 1997 and 2001 flights are presented in § 5.

4. DATA ANALYSIS

4.1. *Event Position and Energy*

The EXITE2 data analysis flowchart is shown in Figure 2. The PMT calibration parameters (i.e., gains and offsets) were first obtained to determine the event position and energy. The calibration events, including the Amcal, LED, and CAL events, can be easily extracted from the data by their validity signatures. A calibration algorithm is then applied to derive the gains and offsets of 49 PMTs (Manandhar 1995). The scintillation light collected by the PMTs can be obtained from its digitized pulse heights and the corresponding gains and offsets. The event positions are first calculated with the simple centroid method from the event light distributions and PMT positions. They are further refined by removing the distortions with the maximum likelihood method (MLM). We used a variant of the MLM proposed by Cook, Finger, & Prince (1985) and Finger (1987) in this analysis. MLM was further developed by Manandhar (1995) and Chou (2001) for the EXITE2 system. The method uses the fact that although the scintillation light from the crystal is proportional to the event energy, all the event energies are corrected by energy "gainmap" (which describes the pulse height–to-energy conversion as a function of position on the detector) because of the dependence of the light collection efficiency on the event positions. Additional details of the MLM and energy gainmap are discussed in Lum et al. (1994), Manandhar (1995), and Chou (2001).

4.2. *Event Selection and Binning*

All the non–X-ray events are filtered out from the observation data before the actual image reconstruction. Some of

[5] Data compression: In order to increase the effective event telemetry rate, only a part of the 49 digitized pulse heights around "peak PMT" (largest pulse height) are transmitted for each event. Seven comparison modes (differing algorithms) could be selected in flight. Approximately uniform PMT gains are required for data compression. Because of the low gain PMTs (PMTs 10 and 47), the data compression was not applied during the EXITE2 1997 flight. The details of the data compression are discussed in Chou et al. (1998) and Chou (2001).

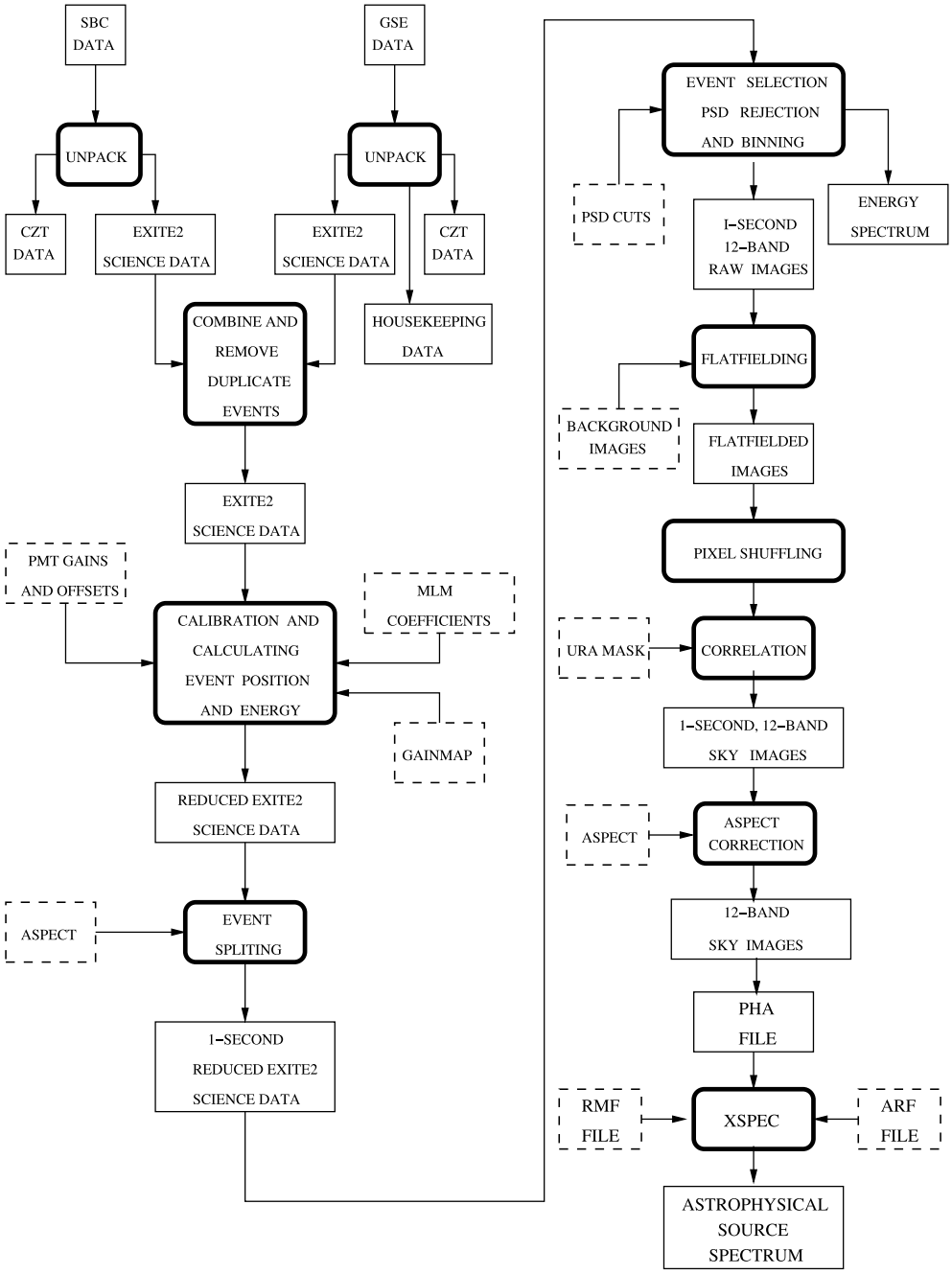

FIG. 2.—Flowchart of the EXITE2 data analysis process

these events, such as shield and charged-particle coincident events are already rejected on board to save telemetry. Others (LED, CAL, and Amcal events) are filtered out through software implementation by making use of their corresponding validity bits recorded in the data.

Because of the PSD energy and position dependence (Chou et al. 1998), the screening process for the CsI(Na) events required slightly more effort than simply relying on hardware rejection. Residual CsI(Na) events that were not rejected by the hardware were screened by making use of the event PSD values. When using the event trigger time as reference, we found that the PSD versus pulse height dependence is significant (Chou et al. 1998). More specifically, the PSD values for a given event depend not only on the scintillation light time constant but also on event energy, PMT gains, and light collection efficiency (gainmap). Thus, they also depend on the event energies and positions. To improve the PSD screening, we divide the events into 49 parts according to the PMT positions. Each part has its own energy-dependent PSD "cut." The PSD [CsI(Na) event] rejection and [NaI(Tl) event] acceptance efficiencies averaged over the whole detector are listed in Table 2. The raw images are accumulated in the 12 logarithmic energy bands from 20 to 600 keV, which are also given in Table 2.

The mask pixel size of EXITE2 is 16 mm $\times$ 16 mm so that event positions are needed to $\leq$8 mm for Nyquist-limited

sampling of the mask shadows for imaging. To further enhance the precision of the source position, the events are binned into 16/6 mm×16/6 mm subpixels (i.e., 6×6 subpixels per mask pixel), although the detector energy-dependent spatial resolution (σ_x(FWHM) $\sim 10.4[E(\mathrm{keV})/60]^{-1/2}$ mm; see Lum et al. 1994) limits this at the lowest energies.

4.3. *Flat-fielding*

The nonuniformities, that is, the systematic deviations in the raw detector image, can create large artifacts in the reconstructed sky images from the coded aperture technique (Laudet & Roques 1988). For the EXITE2 detector, the systematic deviations (from the flight image) arose primarily from the imperfect PSD screening. We expect that the scintillation light of most CsI(Na) events are from the near rear surface of the EXITE2 phoswich, whereas the light of NaI(Tl) events are from closer to the front surface of the crystal. This is due to the finite thickness (3 cm) of the crystal assembly [1 cm NaI(Tl) and 2 cm CsI(Na)]. This gives a difference in the light distributions for CsI(Na) and NaI(Tl) events even when they have an identical event position (x, y). Thus, the MLM coefficients from the 25×25 grid scan (with 60 keV ^{241}Am) of the front surface (Manandhar 1995) are not applicable to the CsI(Na) events. Although the PSD rejection screened out most of the CsI(Na) events, there are still a nontrivial number of residual CsI(Na) events in the data. These residual CsI(Na) events produced a 25×25 grid scan feature of nonuniformities in the derived detector (NaI) image.

To correct the undesirable nonuniformity effects, we applied a subtractive flat-fielding technique, which was originally introduced by Covault (1991) for the EXITE1 detector, to the EXITE2 data. The background images were compiled when the telescope was pointing to a part of the sky, with either no astrophysical source or a weak one, using the same electronic configuration as the source images. The flat-fielded detector image is the source image subtracted by the background image with proper normalization,

$$I_{\mathrm{ff}} = I_s - nI_{\mathrm{bkg}}, \tag{1}$$

where $n = n_s/n_{\mathrm{bkg}}$, and n_s and n_{bkg} are total number of counts for source and background images, respectively. Suppose both source and background images can be written as

$$I_s = \tilde{I}_s + N_s, \tag{2}$$

$$I_{\mathrm{bkg}} = \tilde{I}_{\mathrm{bkg}} + N_{\mathrm{bkg}}, \tag{3}$$

where $\tilde{I}$ is the image "shape," N is the Poisson statistical noise, and the four variables on the right-hand side of equations (2) and (3) are all mutually independent, except $\tilde{I}_s$ and $\tilde{I}_{\mathrm{bkg}}$. Under this construction, the error in the flat-fielded image can be expressed as a quadratic sum of the statistical and the systematic errors,

$$(\sigma_{\mathrm{ff}})^2 = (\sigma_{\mathrm{ff}}^{\mathrm{stat}})^2 + (\sigma_{\mathrm{ff}}^{\mathrm{sys}})^2, \tag{4}$$

where

$$(\sigma_{\mathrm{ff}}^{\mathrm{stat}})^2 = (\sigma_s^{\mathrm{stat}})^2 + n^2(\sigma_{\mathrm{bkg}}^{\mathrm{stat}})^2, \tag{5}$$

$$(\sigma_{\mathrm{ff}}^{\mathrm{sys}})^2 = (\sigma_s^{\mathrm{sys}})^2 + n^2(\sigma_{\mathrm{bkg}}^{\mathrm{sys}})^2 - 2rn\sigma_s^{\mathrm{sys}}\sigma_{\mathrm{bkg}}^{\mathrm{sys}}, \tag{6}$$

and r is the correlation coefficient between $\tilde{I}_s$ and $\tilde{I}_{\mathrm{bkg}}$. Note that when the source and the background images share the same "shape," that is $\tilde{I}_s = n\tilde{I}_{\mathrm{bkg}}$, then in equation (6) $\sigma_s^{\mathrm{sys}} = n\sigma_{\mathrm{bkg}}^{\mathrm{sys}}$, $r = 1$, and $\sigma_{\mathrm{ff}}^{\mathrm{sys}} = 0$. In other words, the flat-fielded image represents an unbiased image of the mask pattern from the astrophysical source with random, uniform statistical noise. A way to test if the systematic error is removed by flat-fielding is the R_{sig} value described in § 4.5.

4.4. *Pixel Shuffling*

The basic uniformly redundant array (URA) mask pattern of EXITE2 contains 13×11 = 143, 1.6 cm×1.6 cm pixels with 72 open and 71 closed. Each mask pixel is a precision-pinned 16 mm×16 mm×12 mm Pb block onto which is bonded a 1 mm thick Sn and 1 mm thick Cu layer for a graded shield. The mask is cyclic and extended in a 2×2 basic pattern (Lum et al. 1994) in order to cover the full detector area. The area of the NaI(Tl) crystal is 36 cm×36 cm = 1296 cm^2, equivalent to 3.54 times that of the basic mask patterns. To enable imaging over the full detector area, we applied the "pixel shuffling" method (Covault 1991) to the EXITE2 data. Because of the cyclic property of the mask, the average counts of any image subpixel in the basic mask pattern can be derived from the average counts of its corresponding subpixels out of the center basic mask pattern and the count in the center basic mask pattern. This creates a "pixel shuffled" image that has the same size as the basic mask pattern but incorporates counts from the full detector, which is then correlated with URA mask to derive the sky counts image.

The pixel shuffling technique produces an average detector counts cm^{-2} image of the detector area being included. Therefore, the signal of the sky image (after correlation), in principle, should be independent of the area size, but the (statistical) noise should of course decrease with larger area. The observation results confirmed that the noise behavior was as we had expected, but interestingly the detected image counts cm^{-2} signal also decreased with larger areas (Chou et al. 1998). In isolating the cause, we discovered that the loss of detector radial sensitivity was due to the gainmap effect[6] combined with the CsI(Na) residual glow induced by the large energy deposition of cosmic ray events so both factors contributed to a decreased spatial resolution at the near edge of detector (Chou et al. 1998). More details about the cosmic ray and gainmap effects are discussed in § 4.5 and Chou (2001).

4.5. *Sky Images and Image Functions*

The balanced correlation method described by Fenimore & Cannon (1978) was applied for sky image reconstruction. The recovered flux (signal) of the image is represented by the maximum correlated value above the mean background level, and the noise is the rms fluctuation of the off-source pixels. Laudet & Roques (1988) showed that the mean fluctuation ΔW of the reconstructed sky image equals the quadratic sum of the detected counts image errors $\Delta P(i, j)$, which for EXITE2 are derived from pixel shuffling as described in § 4.4. That is,

$$(\Delta W)^2 = \sum_{i,j} [\Delta P(i,j)]^2. \tag{7}$$

[6] See eqs. (10) and (11) in § 4.5.

TABLE 3
SKY IMAGE NOISE AND STATISTICAL NOISE OF CYG X-1 OBSERVATION

Energy Band	Energy Range (keV)	rms Noise in Sky Image (counts)	Statistical Noise (counts)	R_{sig}
4	37–50	24.7	23.3	0.95
5	50–70	20.8	20.2	1.03
6	70–93	19.6	19.2	1.02
7	93–127	19.9	20.6	0.97
8	127–174	17.5	18.8	0.93
9	174–237	21.6	22.3	0.97
10	237–323	25.5	26.9	0.97
11	323–440	22.7	21.78	1.04

The statistical error of the pixel-shuffled image may be estimated from Poisson statistics and standard error propagation. We define the ratio R_{sig} to test the goodness of flat-fielding:

$$R_{sig} = \frac{\sigma_{sky}}{\sigma_{shf}^{stat}}, \tag{8}$$

where σ_{sky} is the off-source rms noise of the sky image, which is equivalent to ΔW in equation (7), and σ_{shf}^{stat} is the total statistical error in the pixel-shuffled image. A good flat-fielding result will have little systematic error and $R_{sig} \approx 1$; a bad one would have $R_{sig} > 1$. Table 3 gives the R_{sig} values of the EXITE2 Cyg X-1 observations for energy bands 4 to 11.

If the detector had perfect spatial resolution, the peak counts in the sky image [obtained from a "balanced correlation" (Fenimore & Cannon 1978) of the pixel shuffled detector image and URA mask] would represent the astrophysical source counts detected by the detector. In reality, for a real detector with finite position resolution σ_x, the point spread function (PSF) of the equal balanced correlation image can be written as

$$P_{fin} = G * P_{infin}, \tag{9}$$

where P_{infin} is the PSF for infinite spatial resolution, G is a two-dimensional Gaussian function $\exp(-\boldsymbol{x}^2/2\sigma_{\boldsymbol{x}}^2)/(2\pi\sigma_{\boldsymbol{x}}^2)$, and * is the convolution operator. Clearly, the peak height of P_{fin} is less than the peak height of P_{infin}, unless the Gaussian has $\sigma_{\boldsymbol{x}} = 0$. To recover the source flux, the signal from the sky image must be normalized by the ratio of the PSF heights $[P_{fin}(0,0)/P_{infin}(0,0)$, or the image function].

The image functions for the EXITE2 detector, however, are more complicated than a simple ratio. This is because no unique position resolution ($\sigma_{\boldsymbol{x}}$) can be applied to the whole detector generally because of its position dependence, even for a fixed event energy (see § 4.4 and Chou 2001). To obtain the EXITE2 image functions, we ran a numerical simulation based on the position resolution model described in Chou (2001), that is,

$$\sigma_{\boldsymbol{x}}^2(x,y) = \frac{a}{E_{eff}(x,y)} + \frac{b}{E_{eff}^2(x,y)}, \tag{10}$$

where

$$E_{eff}(x,y) = E \times g(x,y), \tag{11}$$

a and b are constant, E is the scintillation light, and $g(x, y)$ is the gainmap (see § 4.1). In the same way as for the flight images, both the pixel shuffling and the correlation techniques were applied. The image functions were then obtained from the peak height ratios of the correlated images of the finite position resolution from equation (10) versus those with infinite position resolution. Table 4 lists the image functions for the 12 EXITE2 energy bands.

TABLE 4
EXITE2 ENERGY BANDS AND IMAGE FUNCTIONS

Energy Band	Energy Range (keV)	Center Mask Only[a,b]	136×136 Subpixels[a,c]
1	10–20	0.04	0.04
2	20–27	0.11	0.08
3	27–37	0.17	0.13
4	37–50	0.26	0.20
5	50–70	0.37	0.30
6	70–93	0.48	0.40
7	93–127	0.57	0.50
8	127–174	0.65	0.60
9	174–237	0.72	0.68
10	237–323	0.78	0.74
11	323–440	0.82	0.79
12	440–600	0.87	0.84

[a] Detector area used for pixel shuffling.
[b] 13×11 mask pixels $= 78 \times 66$ subpixels.
[c] 136×136 subpixels $= (16/6 \text{ mm})^2 \times 136^2 = (36.2)^2 \text{ cm}^2 \sim$ area NaI crystal ($36 \text{ cm} \times 36 \text{ cm} = 1296 \text{ cm}^2$).

TABLE 5
CYG X-1 OBSERVATION SUMMARY

Observation UT Date	UT Time	Live Time (s)	Total Counts
1997 May 8.....	07:50–09:58	168, 597[a]	3.87×10^5, 1.28×10^6 [a]
2001 May 23.....	08:20–09:54	2182	1.57×10^6

[a] Uncompressed vs. compressed data, respectively; see §§ 3 and 5.1.

4.6. *Spectra*

We analyzed the EXITE2 spectra with the XSPEC[7] (ver. 10.0) implementation for coded aperture imaging given by Bloser et al. (2002). Inputs to the software included the following files: (1) the Pulse Height Analyzer (PHA) data file containing the count spectrum and detector live time, (2) the redistribution matrix file (RMF) describing the instrument response, and (3) the ancillary response file (ARF) containing additional factors for the response as a function of energy such as the collimator response and the atmospheric attenuation. The collimator response in the PHA file captures the pointing offsets and detector live time, which is calculated from the total recovered Amcal events (vs. their laboratory calibration rate of 37 events s^{-1} from all 4 Amcal sources) or CAL events (cf. § 2). The response matrix (RMF file) is constructed by modeling the EXITE2 detector, its surrounding materials, its PSD efficiencies, and its image functions with a Monte Carlo simulation using the MGEANT package (Seifert et al. 1997). The procedural details for generating the EXITE2 spectra are discussed in further detail in Bloser et al. (2002).

5. DATA ANALYSIS RESULTS OF EXITE2 CYG X-1 OBSERVATIONS

5.1. *1997 Observation Results*

Since no SBC data were recorded during the 1997 Cyg X-1 observations, the GSE data constituted the sole data source for our analysis. The total live time and measured counts are summarized in Table 5. The data were processed as prescribed in the analysis flowchart (Fig. 2). Data observed from UT 05:40 to 07:50, when the telescope was pointing on the weak source NGC 4151, were used to construct the background sky images for flat-fielding. The background images have a factor of ~10 more counts than the source images of uncompressed data (observed from UT 07:50 to 08:38, see § 3),[8] so the systematic errors were reduced appreciably after the flat-fielding treatment (i.e., $R_{\rm sig}\sim1$, see Table 3). The additional statistical error contribution due to flat-fielding was less than ~10% (cf. eq. [5], $n\sim\frac{1}{10}$).

The data compression mode changed at UT08:38. The compression scheme was designed for the optimal situation in which all of the PMTs have (approximately) equal gains and offsets. Under such a scenario, the digitized pulse heights observed represent the scintillation light collected by the PMTs. When the PMT gain deviates from this uniformity assumption, the image resolution will be distorted at the local singularities. Unfortunately, during the EXITE2 1997 observation, the gains of PMTs 10 and 47 were only $\frac{1}{2}$ and $\frac{1}{10}$ of the other PMTs' gains, respectively. We found the image distortion near PMT 10 to be minimal but significant near PMT 47 in the compressed data. Fortunately, because PMT 47 is an "edge" PMT (cf. Fig. 1), the distortion is near the boundary of the detector image. In order to avoid the distortion, we extracted only the center basic mask pattern (13×11 mask pixel) images for the analysis instead of applying the pixel shuffling technique. On the other hand, standard pixel shuffling was still applied to the uncompressed data for better signal-to-noise ratio. Although the pointing was stable, with pointing offsets less than 30′ during the observations, the aspect correction described by Covault (1991) was applied to our data analysis to precisely measure the astrophysical source counts.

The detector live times were 168 s for the first (uncompressed data) and 597 s for the second (compressed data) parts of observation, respectively. The source was detected in energy bands 4 through 9 (37–237 keV). Figure 3 shows the image contour plot of 93–127 keV (band 7) from the uncompressed data, in which the source is detected at 8.6 σ. Two models were applied for spectral fitting: the single-temperature Comptonization model (CompST model in XSPEC) described by Sunyaev & Titarchuk (1980) and the more sophisticated Comptonization model of Titarchuk (1994, CompTT model in XSPEC), which takes into account relativistic effects and is valid for both optically thick and thin plasmas. A spherical geometry was assumed for both models. Both models gave similar parameters when applied to the uncompressed and compressed data individually, although the fit for the uncompressed data was formally unacceptable

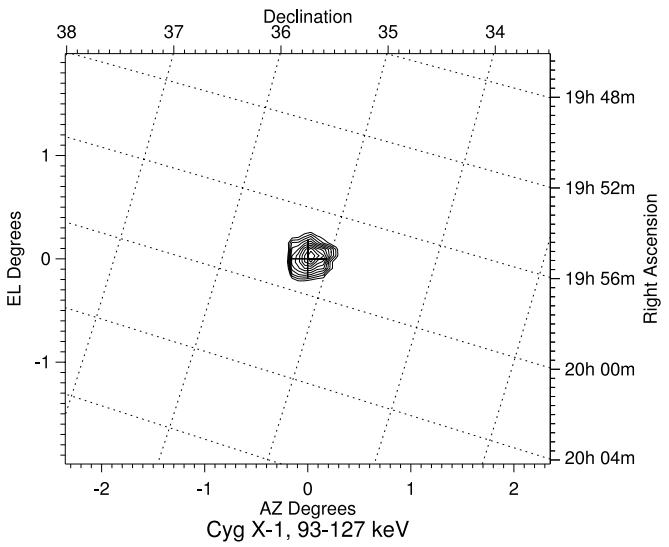

FIG. 3.—EXITE2 image of the black hole binary Cyg X-1 in the energy range 93–127 keV (band 7), detected with a significance of 8.55 σ in the 168 s of detector live time from the first data set. Contours represent detection significance and scale from 3.0 σ to 9.0 σ in steps of 0.5 σ.

[7] XSPEC: X-ray spectral analysis software is available from http://heasarc.gsfc.nasa.gov/docs/xanadu/xanadu.html.

[8] The data for flat-fielding contain both SBC and GSE data.

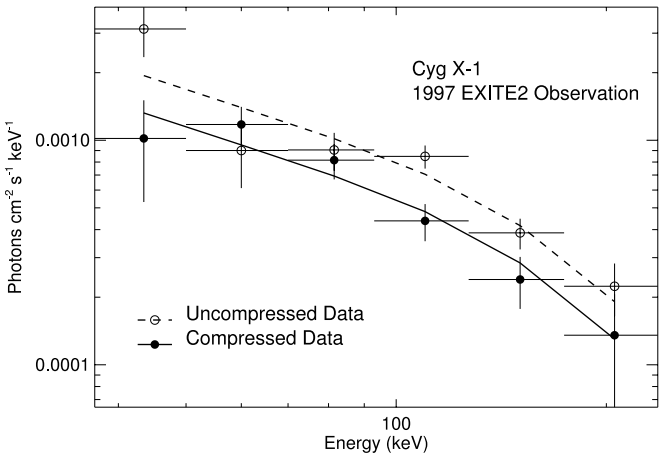

FIG. 4.—1997 EXITE2 spectra of Cyg X-1 with single-temperature Comptonization (CompTT model) fit. Both the 168 s of uncompressed data (*open circles*) and the 597 s of compressed data (*filled circles*) were fit simultaneously with only the normalization allowed to vary. Best-fit parameters are $kT_e = 42.9^{+13.9}_{-7.3}$ keV and $\tau = 6.5^{+2.5}_{-1.6}$, with $\chi^2_\nu = 11.1/7 = 1.58$. The normalization of the compressed data fit (*solid line*) is 0.68 times that of the uncompressed data fit (*dashed line*). This variation takes place over ~10 minutes.

because of the low statistics and large deviation in the second energy bin. We therefore fit both data sets simultaneously, allowing only the normalization to vary. This gave acceptable and similar fits for both models, with best-fit parameters $kT_e = 44.6^{+13.2}_{-8.9}$ keV, $\tau = 4.4^{+2.7}_{-1.1}$, and $\chi^2_\nu = 11.1/8 = 1.39$ for the CompST model and $kT_e = 42.9^{+13.9}_{-7.3}$ keV, $\tau = 6.5^{+2.5}_{-1.6}$, and $\chi^2_\nu = 11.1/7 = 1.58$ for the CompTT model (errors are 1 σ). The normalization of the compressed data was 0.68 times that of the uncompressed data. Figure 4 shows the EXITE2 spectra for the uncompressed and compressed data between 37 and 237 keV, together with the best-fit CompTT model. The best-fit parameters are summarized in Table 6.

The spectral parameters indicate that Cyg X-1 was in its normal low state during the EXITE2 observation. The *RXTE* ASM light curve (2–12 keV) for the time period in question supports this conclusion as well (~0.35 crab, see Fig. 5 and Ling et al. 1997). More precisely, the spectral parameters are indicative of the γ_3 state of Ling et al. (1987). The EXITE2 flux, however, seems rather more in keeping with that expected for the dimmer γ_1 state: 5.2×10^{-4} and 3.5×10^{-4} photons cm^{-2} s^{-1} keV^{-1} at 100 keV for the first and the second data sets, respectively (compare to Ling et al. 1997). The cause of this discrepancy is unknown; during the same flight, spectral fits to the Crab yielded the correct normalization at 100 keV (Bloser et al. 2002). Figure 4 indicates that the hard X-ray flux of Cyg X-1 is variable by ~30% on timescales on the order of 10 minutes. Such rapid variability might be expected from a wind-fed accretion source like Cyg X-1 if the hot corona is fed directly by a quasi-spherical accretion flow, instead of via evaporation from the accretion disk, which reacts over the much longer viscous timescale. A two-flow accretion model consisting of a Keplerian accretion disk and a sub-Keplerian (i.e., free-falling) flow has been proposed by Chakrabarti & Titarchuk (1995), and recent long-term monitoring of the broadband spectra of a number of sources has lent support to this picture (Smith, Heindl, & Swank 2002). The idea is that in a low-mass binary system, which has a large accretion disk because of Roche lobe overflow, changes in the accretion rate will make themselves evident in the hard X-ray band, in which they propagate over a free-fall timescale, far more rapidly than in the soft X-ray band, in which changes must move through the disk over the viscous timescale. This behavior is observed in many low-mass systems (Smith et al. 2002). In a high-mass, wind-fed system like Cyg X-1, the accretion disk is much smaller and so reacts much more quickly, but over timescales of tens of minutes, a lag at low energies might still be evident. Simultaneous soft X-ray observations would be necessary to confirm this scenario.

5.2. *2001 Observation Results*

A data analysis process similar to that for the 1997 observations was applied to the 2001 data. Thanks to the extremely stable pointing system developed by the High-Energy Replicated Optics (HERO) group at Marshall Space Flight Center (MSFC) (our collaborators), the aspect fluctuation was less than 4′ (~1 subpixel) for most (>97%) of the time. Therefore, no aspect correction was necessary for data analysis. The total data throughput measured by the CAL events was 39%, and the detector live time was 2181 s. Figure 6 shows the image contour plot of 37–237 keV (sum of band 4 to band 9) of the observations, in which the source detection is 20.96 σ. As for the 1997 data, the CompST and CompTT models were applied to the spectral data. In both cases the spectral parameters were far less well constrained than for the 1997 observation. The CompST fit gave only $kT_e > 47.6$ keV, $\tau = 1.5^{+0.78}_{-0.94}$, and $\chi^2_\nu = 1.52/3 = 0.51$, and the CompTT fit

TABLE 6
SUMMARY OF THE EXITE2 SPECTRAL FITS TO CYG X-1

Observation	Model	kT_e[a] (keV)	τ[b]	α[c]	F_{100}[d] (photons cm^{-2} s^{-1} keV^{-1})	χ^2_ν
1997.....	CompST	$44.6^{+13.2}_{-8.9}$	$4.4^{+2.7}_{-1.1}$	...	...	1.39
	CompTT	$42.9^{+13.9}_{-7.3}$	$6.5^{+2.5}_{-1.6}$	...	(5.2, 3.5) $\times 10^{-4}$ [e]	1.58
2001.....	CompST	>47.6	$1.5^{+0.78}_{-0.94}$	...	...	0.51
	CompTT	>51.7	$0.87^{+2.02}_{-0.84}$	...	...	0.40
	Power Law	...	...	$2.27^{+0.09}_{-0.10}$	4.2×10^{-4}	0.48

NOTE.—Errors are 1 σ for the parameter of interest.
[a] Comptonizing electron temperature.
[b] Comptonizing electron optical depth.
[c] Power-law photon index.
[d] Flux at 100 keV.
[e] Uncompressed vs. compressed data, respectively; see §§ 3 and 5.1.

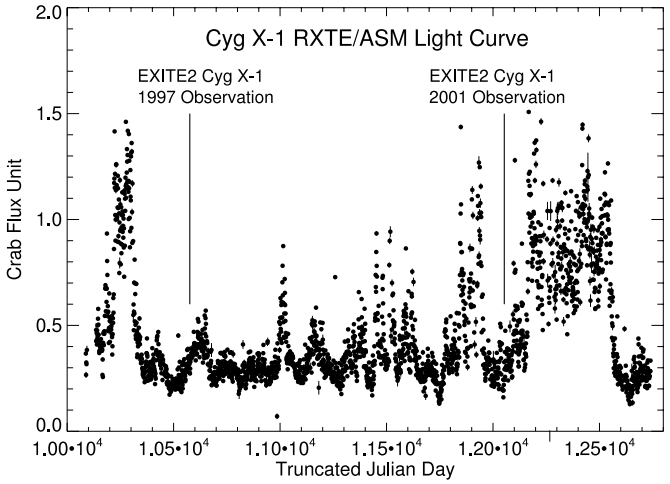

FIG. 5.—Cyg X-1 flux history (1 day averages) detected by *RXTE* ASM (2–10 keV). The flux during the 1997 EXITE2 observation on 1997 May 8(= TJD 10576) and the 2001 EXITE2 observation on 2001 May 24 (= TJD 12053) were ~0.35 and ~0.31 crab (1 crab = 74 counts s^{-1} for *RXTE* ASM), respectively. Note the switch to the high state shortly after the 2001 observation.

gave $kT_e > 51.7$ keV, $\tau = 0.87^{+2.02}_{-0.84}$, and $\chi^2_\nu = 1.24/2 = 0.4$. In fact, the best fit was for a simple power law with photon index $\alpha = 2.27^{+0.09}_{-0.10}$ ($\chi^2_\nu = 1.91/4 = 0.48$). This power-law fit is shown in Figure 7, and the fits for all three models are summarized in Table 6. These fits indicate that the spectral break was at too high an energy to be constrained by the EXITE2 observation, which was only sensitive up to 237 keV.

There are two possible interpretations of this result. The spectral data, together with the derived flux at 100 keV of 4.2×10^{-4} photons cm^{-2} s^{-1} keV^{-1}, could indicate that Cyg X-1 was observed in the dim γ_1 state. Typical electron temperatures for this state are $kT_e \sim 80$–100 keV (Ling et al. 1987, 1997), too high to be constrained with the current EXITE2 data. However, the *RXTE* ASM light curve indicates

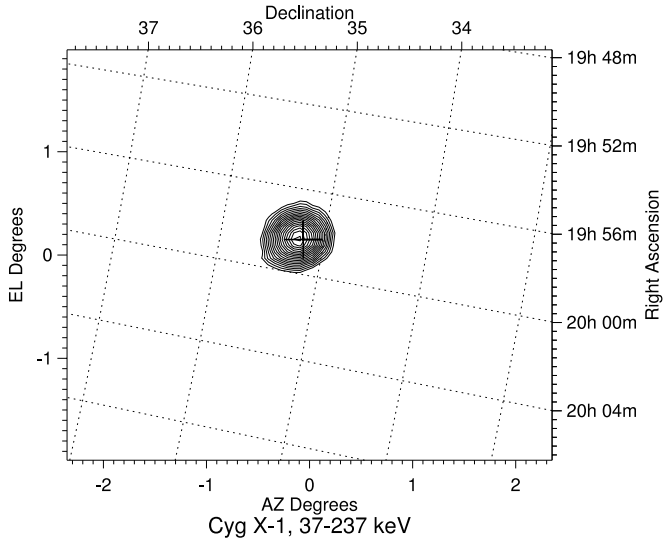

FIG. 6.—EXITE2 image of the black hole binary Cyg X-1 from the 2001 observation in the energy range 37–237 keV (Band 4 to 9), detected with a significance of 20.96 σ. Contours represent detection significance and scale from 3.5 σ to 21.0 σ in steps of 1.0 σ. The cross near the center indicates the expected source centroid.

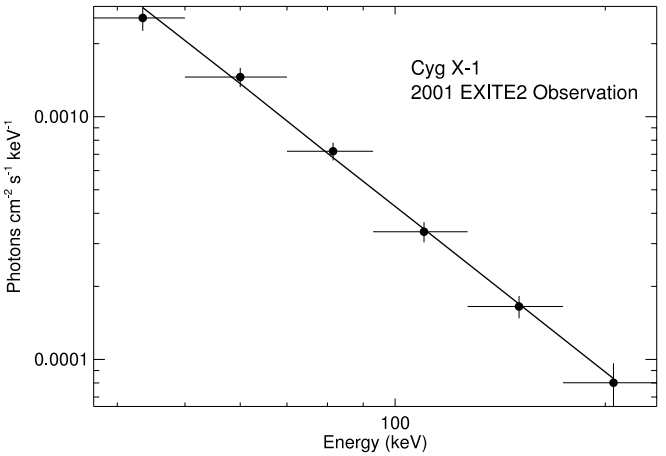

FIG. 7.—EXITE2 spectrum of Cyg X-1 observed in the 2001 flight with a power-law fit. The best fit gives photon index $\alpha = 2.27^{+0.09}_{-0.10}$ and $\chi^2_\nu = 0.48$. No spectral break could be constrained, indicating either the low γ_1 state or the high state.

that Cyg X-1 made a transition to the high state shortly after the EXITE2 observation (Fig. 5). Thus the observed soft power law with no apparent cutoff is more likely an indication of the transition to the high state, as such a hard X-ray spectrum is typical of black hole X-ray binaries in the high state (Grove et al. 1998; Esin et al. 1998). The model of Chakrabarti & Titarchuk (1995) discussed above does predict a soft extended power law in the high state as the result of bulk Comptonization of soft photons off the free-falling, converging flow. This model, however, predicts a sharp spectral cutoff below 500 keV (Laurent & Titarchuk 1999), whereas broadband observations of Cyg X-1 in the high state indicate power-law emission extending to well above 1 MeV (McConnell et al. 2002). We note that this broadband observation encompassed 11 days and so would not be sensitive to spectral variations on shorter timescales. Nevertheless, hybrid models involving Comptonization by both thermal and nonthermal electrons can also fit the high-state spectrum of Cyg X-1 from 0.5 keV to $\geq$5 MeV (McConnell et al. 2002). It is clear that more sensitive instruments in the MeV band are needed to further constrain the models.

The EXITE2 spectral parameters for single-temperature Comptonization fits are compared to those found for the low state of Cyg X-1 by other hard X-ray instruments in Table 7. The best-fit Comptonization parameters for the 2001 observation are included for completeness.

6. CONCLUSIONS

The EXITE2 telescope has successfully observed several astrophysical sources during its 1997 and 2001 flights. In this paper, we reported the development of the EXITE2 data analysis methods, including PSD rejection, flat-fielding, image function, and spectral analysis. The EXITE2 Cyg X-1 spectra give reasonable Comptonization parameters with the source in the normal low state for the 1997 observation, and a typical high-state power law for the 2001 observation. Evidence of hard X-ray variability on the free-fall timescale is seen. The Crab Nebula spectrum is also consistent with those from other hard X-ray instruments, with a power index of 2.36 ± 0.33 (Bloser et al. 2002). The EXITE2 3C 273/GRS 1227+025 observation results are reported in a separate paper (Grindlay et al. 2005).

TABLE 7

SINGLE-TEMPERATURE COMPTONIZATION PARAMETERS OF CYG X-1 IN LOW STATE FROM EXITE2 AND OTHER HARD X-RAY INSTRUMENTS

Instrument	Energy Range for Fit (keV)	kT_e (keV)	τ	Reference
MPI/AIT	15–200	27	5	1
*HEAO*1	3–300	32.4 ± 0.4	3.99 ± 0.01	2
MISO	28–300	50 ± 17	$2.5^{+1.1}_{-0.9}$	3
*HEAO*3	48–300	$42.0^{+4.1}_{-4.3}$	$2.8^{+0.41}_{-0.30}$	3
SIGMA	35–750	62.3 ± 4.5	2.02 ± 0.13	4
SIGMA	60–600	57 ± 2	0.73 ± 0.03	5
BATSE	25–300	53.1	2.68	6
BATSE	25–300	55.7	2.73	6
EXITE2 (1997)	40–237	$42.9^{+13.9}_{-7.3}$	$6.5^{+2.5}_{-1.6}$	7
EXITE2 (2001)	40–237	> 51.7	$0.87^{+2.02}_{-0.84}$	7

REFERENCES.—(1) Sunyaev & Trümper 1979; (2) Nolan et al. 1981; (3) Perotti et al. 1986; (4) Salotti et al. 1992; (5) Grebenev et al. 1993; (6) Ling et al. 1997; (7) this paper.

The authors thank T. Gauron, J. Gomes, V. Kuosmanen, F. Licata, G. Nystrom, A. Roy, and R. Scovel (SAO) for their engineering support, G. Monnelly for invaluable technical assistance, J. Grenzke, M. Perrin, and B. Robbason for SBC development, the staff of the National Scientific Balloon Facility (NSBF) for their balloon launches and excellent flight operations support, and the HERO group in MSFC for their developing the gondola for the 2001 flight. P. F. B. acknowledges a National Research Council Research Associateship at GSFC. T. N. acknowledges support from the College of the Holy Cross. This work was partially supported by NASA grants and NAG5-5103 and NAG5-5279.

REFERENCES

Bloser, P. F. 2000, Ph.D. thesis, Harvard University
Bloser, P. F., Chou, Y., Grindlay, J. E., Narita, T., & Monnelly, G. 2002, Astropart. Phys., 17, 393
Caroli, E., Stephen, J. B., Cocoo, G. D., Natalucci, L., & Spizzichino, A. 1987, Space Sci. Rev., 45, 349
Chakrabarti, S. K., & Titarchuk, L. G. 1995, ApJ, 455, 623
Chou, Y. 2001, Ph.D. thesis, Harvard University
Chou, Y., Bloser, P. F., Grenzke, J., Grindlay, J.E., Lum, K. S. K., Monnelly, G., & Robbason, B. 1998, in IEEE Nuclear Science Symposium Conference Record (Piscataway: IEEE), 210
Cook, W. R., Finger, M., & Prince, T. A. 1985, IEEE Trans. Nucl. Sci., NS-32, 129
Covault, C. E. 1991, Ph.D. thesis, Harvard University
Esin, A. A., Narayan, R., Cui, W., Grove, J. E., & Zhang, S.-N. 1998, ApJ, 505, 854
Fenimore, E. E., & Cannon, T. M. 1978, Appl. Opt., 17, 337
Finger, M. 1987, Ph.D. thesis, California Institute of Technology
Grebenev, S. et al. 1993, A&AS, 97, 281
Grindlay, J. E., Chou, Y., Bloser, P. F., & Narita, T. 2005, ApJ, 618, 852
Grove, J. E., Johnson, W. N., Kroeger, R. A., McNaron-Brown, K., Skibo, J. G., & Phlips, B. F. 1998, ApJ, 500, 899
Laudet, P., & Roques, J. P. 1988, Nucl. Instrum. Methods Phys. Res., A267, 212
Laurent, P., & Titarchuk, L. 1999, ApJ, 511, 289
Ling, J. C., Mahoney, W. A., Wheaton, W. A., & Jacobson, A. S. 1987, ApJ, 321, L117
Ling, J. C., Wheaton, W. A., Wallyn, P., Mahoney, W. A., Paciesas, W. S., Harmon, B. A., Fishman, G. J., Zhang, S. N., & Hua, X. M. 1997, ApJ, 484, 375
Lum, K. S. K., Manandhar, R. P., Eikenberry, S. S., Krockenberger, M., & Grindlay, J. E. 1994, IEEE Trans. Nucl. Sci., NS-41, 1354
Manandhar, R. P. 1995, Ph.D. thesis, Harvard University
McConnell, M. L., et al. 2002, ApJ, 572, 984
Nolan, P. L., Gruber, D. E., Knight, F. K., Matteson, J. L., Rothschild, R. E., Marshall, F. E., Levine, A. M., & Primini, F. A. 1981, Nature, 293, 275
Paul, J., et al. 1991, Adv. Space Res., 11, 289
Perotti, F., della Ventura, A., Villa, G., Bassani, L., Butler, R. C., di Cocco, G., Baker, R. E., Dean, A. J., & Hanson, C. G. 1986, ApJ, 300, 297
Priedhorsky, W. C., Terrell, J., & Holt, S. S. 1983, ApJ, 270, 233
Salotti, L., et al. 1992, A&A, 253, 145
Schindler, S. M., Cook, W. R., Hammond, J., Harrison, F. A., Prince, T. A., Song, W., Corbel, S., & Heindl, W. A. 1997, Nucl. Instrum. Methods Phys. Res., 384, 425
Seifert, H., Naya, J. E., Sturner, S. J., & Teegarden, B. J. 1997, in AIP Conf. Proc. 410, Proceedings of the Fourth Compton Symposium, ed. C. D. Dermer, M. S. Strickman, & J. D. Kurfess (New York: AIP), 1567
Smith, D. M., Heindl, W. A., & Swank, J. H. 2002, ApJ, 569, 362
Sunyaev, R. A., & Titarchuk, L. G. 1980, A&A, 86, 121
Sunyaev, R. A., & Truemper, J. 1979, Nature, 279, 506
Titarchuk, L. 1994, ApJ, 434, 570